sciendo

GEOLOGOS

Geologos 27, 3 (2021): 157–172
DOI: 10.2478/logos-2021-0018

Assessing the representative elementary volume of rock types by X-ray computed tomography (CT) – a simple approach to demonstrate the heterogeneity of the Boda Claystone Formation in Hungary

Saja M. Abutaha[1*], János Geiger[1], Sándor Gulyás[1], Ferenc Fedor[2]

[1] University of Szeged, Department of Geology and Paleontology, Egyetem utca 2-6, 6722 Szeged, Hungary;
e-mails: JG: matska@geo.u-szeged.hu, SG: gulyas.sandor@geo.u-szeged.hu
[2] GEOCHEM Ltd, 55/1 Viola Str, 7761 Kozármisleny, Hungary; e-mail: fedor.ferenc@geochem-ltd.eu
* corresponding author, e-mail: sajaabutaha@geo.u-szeged.hu

Abstract

X-ray computed tomography (CT) can reveal internal, three-dimensional details of objects in a non-destructive way and provide high-resolution, quantitative data in the form of CT numbers. The sensitivity of the CT number to changes in material density means that it may be used to identify lithology changes within cores of sedimentary rocks. The present pilot study confirms the use of Representative Elementary Volume (REV) to quantify inhomogeneity of CT densities of rock constituents of the Boda Claystone Formation. Thirty-two layers, 2 m core length, of this formation were studied. Based on the dominant rock-forming constituent, two rock types could be defined, i.e., clayey siltstone (20 layers) and fine siltstone (12 layers). Eleven of these layers (clayey siltstone and fine siltstone) showed sedimentary features such as, convolute laminations, desiccation cracks, cross-laminations and cracks. The application of the Autoregressive Integrated Moving Averages, Statistical Process Control (ARIMA SPC) method to define Representative Elementary Volume (REV) of CT densities (Hounsfield unit values) affirmed the following results: i) the highest REV values corresponded to the presence of sedimentary structures or high ratios of siltstone constituents (> 60%). ii) the REV average of the clayey siltstone was (5.86 cm^3) and (6.54 cm^3) of the fine siltstone. iii) normalised REV percentages of the clayey siltstone and fine siltstone, on the scale of the core volume studied were 19.88% and 22.84%; respectively. iv) whenever the corresponding layer did not reveal any sedimentary structure, the normalised REV values would be below 10%. The internal void space in layers with sedimentary features might explain the marked textural heterogeneity and elevated REV values. The drying process of the core sample might also have played a significant role in increasing erroneous pore proportions by volume reducation of clay minerals, particularly within sedimentary structures, where authigenic clay and carbonate cement were presumed to be dominant.

Key words: Hounsfield Unit (HU), Autoregressive Integrated Moving Averages (ARIMA), Statistical Process Control (SPC) technique

1. Introduction

In the early 1970s, the Hounsfield's X-ray CT prototype (Hounsfield, 1973) generated tremendous excitement within the medical community. The CT, or CAT, was the first imaging modality to allow accurate, non-destructive interior image reconstruction of an object from a sufficient number of X-ray projections, i.e., reconstructions of 3D bones and soft-tissue images.

In view of the fact that CT proved to be able to reveal precisely and accurately the spatial distribution of the inner structure of objects examined and provide unrivalled information about materials from scale lengths of metres, down to tens of nanometres, CT application has become unlimited. As a consequence, numerous geoscientific studies incorporate CT scan analysis, such as investigations of soil moisture content, mineralisation layers in manganese nodules, local structure of marine sedimentary rocks or coal composition. Such methods were also applied to study the mechanical rock properties, and residual oil distribution in carbonate or clastic cores (e.g., Garvey & Hanlon, 2002; Sutton et al., 2002; Van Kaick & Delorme, 2005; Cnudde et al., 2006; Louis et al., 2007). In addition, complexities of geological formations, including bedding features, sedimentary structures and coring-induced fractures, cement distribution, small-scale grain size variations and density variation at scales of core samples have been analysed by using this technique (e.g., Coles et al., 1991, 1998). CT scanning is also employed to determine the quality of subsurface materials (e.g., heterogeneity, damages, presence of fluids) and to gain insight into physical properties of cores (bulk density, porosity and fluid saturations) (Coles et al., 1991; Cnudde et al., 2013; Gang et al., 2019). Efforts have also been made to use CT scanning in order to understand fluid displacement and relative permeability of core material from reservoirs (Hove et al., 1987; Vinegar & Wellington, 1987; Withjack, 1988).

The scale of observation is a fundamental aspect in modelling material behaviour or deriving its effective macroscale parameters from the constituent relations governed by the spatial distribution of its components. Any given sample (i.e., rock sample) can be considered homogeneous when the scale of observation is large enough to obtain constant parameters of concern (Russo & Jury, 1987; Webster, 2000). Various geological processes such as deposition, diagenesis, erosion and structural deformation that ultimately control the geometry of sedimentary deposits leads to heterogeneity in rock bodies (Brown et al., 2000). Accurate determination of rock heterogeneity is critical for a variety of industrial applications. For instance, it plays a key role in determining the reservoir's ability to recover oil and gas (Russo & Jury, 1987; Chang & Gao, 1995; Muhlhaus & Oka, 1996; Webster, 2000), carbon geostorage efficiency (Feyel & Chaboche, 2000; Peerlings & Fleck, 2001; Kouznetsova et al., 2001, 2002), contaminant mitigation and natural source zone depletion (Bear & Bachmat, 1990; Clausnitzer & Hopmans, 1999), water discharge and extraction rates (Brown et al., 2000; Baveye et al., 2002) or geothermal energy production feasibility (e.g., Al-Raoush & Willson, 2005). It is thus essential to understand rock heterogeneity in detail so as to make reliable predictions or process optimisation.

One of the methods for quantifying heterogeneity is to use the Representative Elementary Volume (REV (Fig. 1). The REV of a rock mass is defined as the smallest volume over which the studied parameter (in this case, density), yields a constant value (Long et al., 1982; Shapiro & Andersson, 1983; Blum et al., 2007). The present study aims to quantify and evaluate the minimum volume of a core sample of the of Boda Claystone Formation (Permian, S Hungary), that can capture a representative quantity of its physical heterogeneity (i.e., density). Three major routes were followed to fulfil the above target: i) based on the dominant rock-forming components, rock types were detected as consecutive thin layers; the average HU (Hounsfield Unit) of rock constituents was calculated for each of these, ii) the ARIMA SPC technique was applied to compute REV

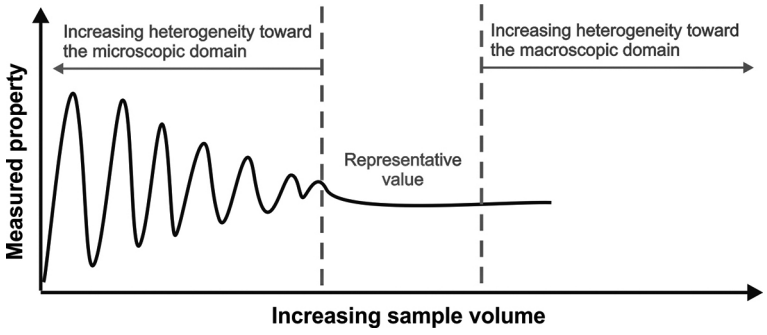

Fig. 1. Definition of the Representative Elementary Volume, REV (after Bear, 1972).

values of layers defined, iii) Computed REV values were generalised using the Monte-Carlo simulation method.

2. CT scans: basic principles and applications

2.1. CT principle

The theoretical foundations of computed tomography (CT) were established by Cormack & Hounsfield (1989). Subsequent developments in CT technology have led to the introduction of new instruments, such as spiral CT (1989), multi-slice CT, micro-CT, nano-CT (1998) and multi-slice CT with double X-ray tubes (Garvey & Hanlon, 2002).

CT measures the X-ray linear attenuation coefficient of an object from different directions and produces several cross-sectional images of the volume measured. The linear attenuation coefficient is a function of both electron density (bulk density) and the effective atomic number. Akin & Kovscek (2003) pointed out that for X-ray energies above 100 kV, the CT image was proportional to density and for those well below 100 kV, it was proportional to effective atomic number.

A single CT scan image is produced using a mono-energetic X-ray. As each X-ray beam passes through the sample, it attenuates varyingly, and the transmitted X-ray is received by a detector (Hounsfield, 1973). The X-ray attenuation depends on X-ray energy and effective atomic density of the sample and can be determined using Beer Lambert's law (Equation (1)). Each rotation of the X-ray source around the sample produces a cross-sectional image, which can then be stacked to form a 3D volume.

$$I = I_0 \, e^{-(\mu d)} \tag{1}$$

where I is the intensity of the transmitted X-ray, Io is the initial X-ray intensity, μ is the linear X-ray attenuation coefficient and d is the length of the X-ray path inside the object. When X-ray energy and intensity are kept constant, linear attenuation of X-ray occurs as a function of density, resulting in sensitivity of CT images to density changes (Heismann et al., 2003; Duchesne et al., 2009). Series of X-ray attenuation measurements are numerically processed (reconstructed) so as to show the spatial distribution of X-ray attenuation coefficients within the sample.

The signal at each point in the reconstructed images, referred to as the CT number, is expressed in Hounsfield units. The Hounsfield unit (HU) scale is a linear transformation of the original linear attenuation coefficient measurement into one in which the radiodensity of distilled water at standard pressure and temperature (STP) is defined as zero Hounsfield units (HU), while the radiodensity of air at STP is defined as −1000 HU. The corresponding HU value is therefore given by:

$$HU = 10^3 \times \frac{\mu - \mu_w}{\mu_w} \tag{2}$$

where μ is the attenuation coefficient of the measured material, μ_w being the attenuation coefficient of water. Each Hounsfield unit (HU) represents a 0.1% change in density with respect to the calibration density scale. If the measurement is calibrated to water, this yields HU=0 for water and HU =−1000 for air.

The default output of a CT scan is a grey-scale 2D image. In such an image, each pixel contains an HU-value associated with the average density and composition of the material in a given volume behind the pixel. From these scans, a 3D-tomographic image can be generated (e.g., Herman, 2009).

In general, tomography is a technique that generates a data set (images), called a tomogram, which is a three-dimensional representation of the structure and variation of composition within a rock specimen. Each 3D element in the tomogram is called a voxel and contains an average coefficient value (HU). Voxel size equals pixel size by slice thickness. The resolution of the CT image produced depends on the scanner used. Fine details can be detected from the highest resolution. CT image resolution or spatial resolution is estimated by measuring the two nearest distinguishable objects in a two-dimensional CT image (Taud et al., 2005; Herman, 2009).

Measurements with X-ray CT are subject to a range of errors and image artifacts, including Beam hardening, star-shaped, positioning error and machine error. These artifacts and the techniques used to minimise them were discussed in full by Van Geet et al. (2000), Ketcham & Carlson (2001) and Akin & Kovscek (2003).

With a given attenuation data set (tomographic image), images can be further manipulated by changing the viewable window settings in order to accentuate specific contrast differences (Földes et al., 2004; Wesolowski & Lev, 2005; Földes, 2011). Another essential feature of these types of analyses is the availability of a quantitative background data set that can be analysed by applying various statistical or geostatistical methods.

2.2. Applied CT scans

CT measurements of about 2 m-long core samples were performed on a Siemens Emotion 6 medical scanner at the Institute of Diagnostic Imaging and Radiation Oncology, University of Kaposvar, Hungary. The instrument operates at 120 kVp (peak kilovoltage), with 250 mAs (milliampere-seconds) current, 1.0 s (sampling intervals). The lateral resolution was (0.1953 x 0.1953) mm^2 with 1.25 mm of scan-slice thickness. The image reconstruction matrix was 512 x 512 pixels. The field of view (FOV) was approximately 9.99 cm. CT images are stored in a DICOM (Digital and Imaging Communications in Medicine) format. A DICOM file contains in its metadata the scanning parameters and scanned object identification under different attributes. Of these metadata, the *PixelSpacing* and *SliceThickness* attributes are important for geoscientific applications as they record the dimension (in millimetres) of each voxel in the x, y, and z-direction. Each CT number can be assigned a real-world distance (or depth), allowing CT number profiles to be constructed so that depth and geometrical measurements can be calculated. DICOM images are be easily read by 'classical' 3D volume rendering softwares (Abutaha et al., 2021).

Scans were made using a modified dual-scanning approach (Balázs et al., 2018). The dry core material was first placed in a vacuum tube. After six hours of vacuuming, whole-core CT scans were made (dry condition). In the next step, the core material was saturated with water. After one hour of relaxation, the scanning process was repeated in the same position of the same measured slice (flooded or evacuated condition). The laboratory guaranteed that the DICOM files were free of any artifacts and that during the second scan the same pixels were measured as during the first one. For the present paper, we focused on the analysis of vacuumed (dry) scanned slices alone.

3. Core sample: location and lithology

The rock formation studied belongs to the Permian fluvial sedimentary sequence named the Boda Claystone Formation (BCF), which is situated in the western Mecsek Mountains of southern Transdanubia (southern Hungary) (Fig. 2) and covers an area of 150 km^2, ten per cent of which is found in outcrop. Low porosity, appropriate hydraulic conductivity and absence of organic residues are characters which favoured the BCF as a potential disposal repository rock formation for high-level nuclear waste (HLW) in Hungary. The BCF was deposited in a shallow-water, salt-lake environment sur-

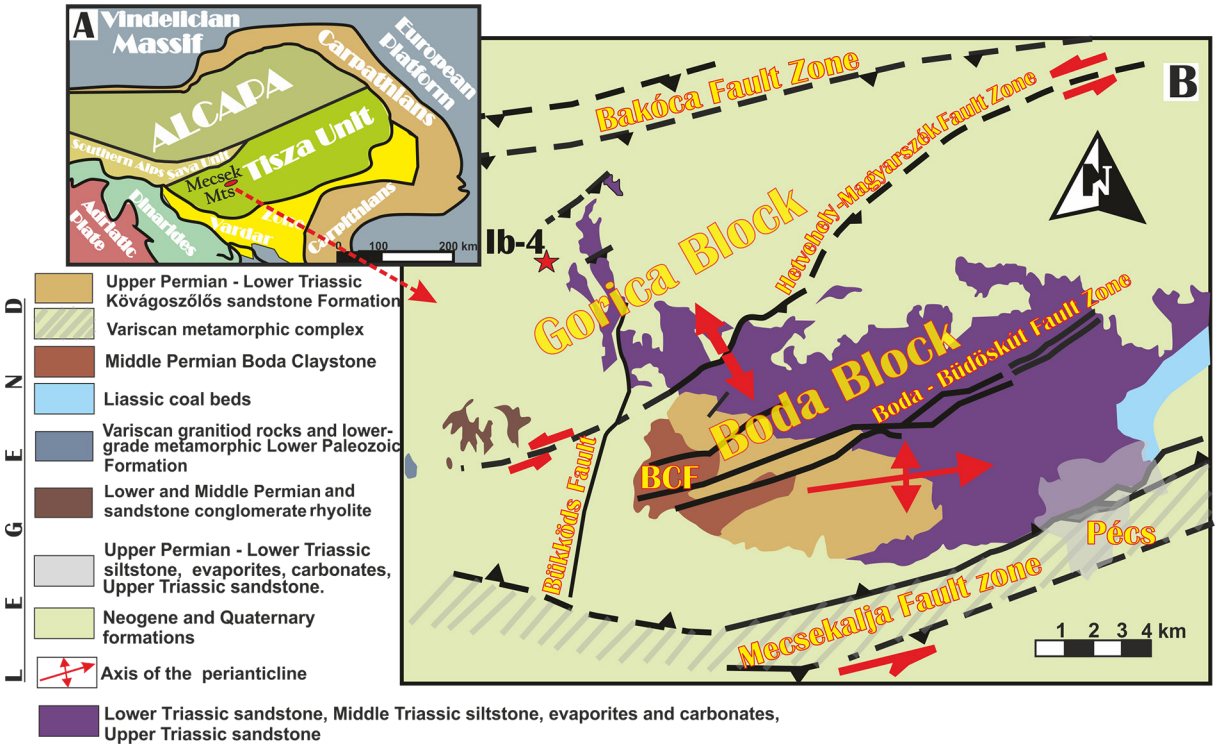

Fig. 2. A – Distribution of Boda Claystone Formation sequences in the Mecsek Hills area (after Haas & Péró, 2004); **B –** The studied core site, Ibafa 4 (Ib-4), marked by a red star in the upper left-hand corner.

rounded by dry to saline mudflats under semi-arid to arid climatic conditions (Barabás & Barabás-Stuhl, 1998; Máthé, 1998; Árkai et al., 2000; Varga et al., 2005; Máthé & Varga, 2012).

The BCF has two outcrop distributional areas: the western Mecsek mountain (a peri-anticlinal structure) and the Gorica block. In the latter area, a single borehole (Ib-4), which reached a depth of *c.* 200 m, is available for detailed studies. Recent stratigraphical studies have shown that the BCF, generally speaking, starts with fine-grained sandstone beds at the base; these are overlain by albitic claystone/siltstone, with successive claystone, albitic clayey siltstone and silty claystone with dolomite at the top (Konrád et al., 2010). The underlying Cserdi Formation (Upper Permian) consists mainly of reddish-brown conglomerate, unsorted, matrix-supported sandstone and siltstone beds, representing debris flow-dominated alluvial deposits (Barabás & Barabás-Stuhl, 1998). The stratigraphical position of the core sample studied within the entire cored sections is shown in Figure 3.

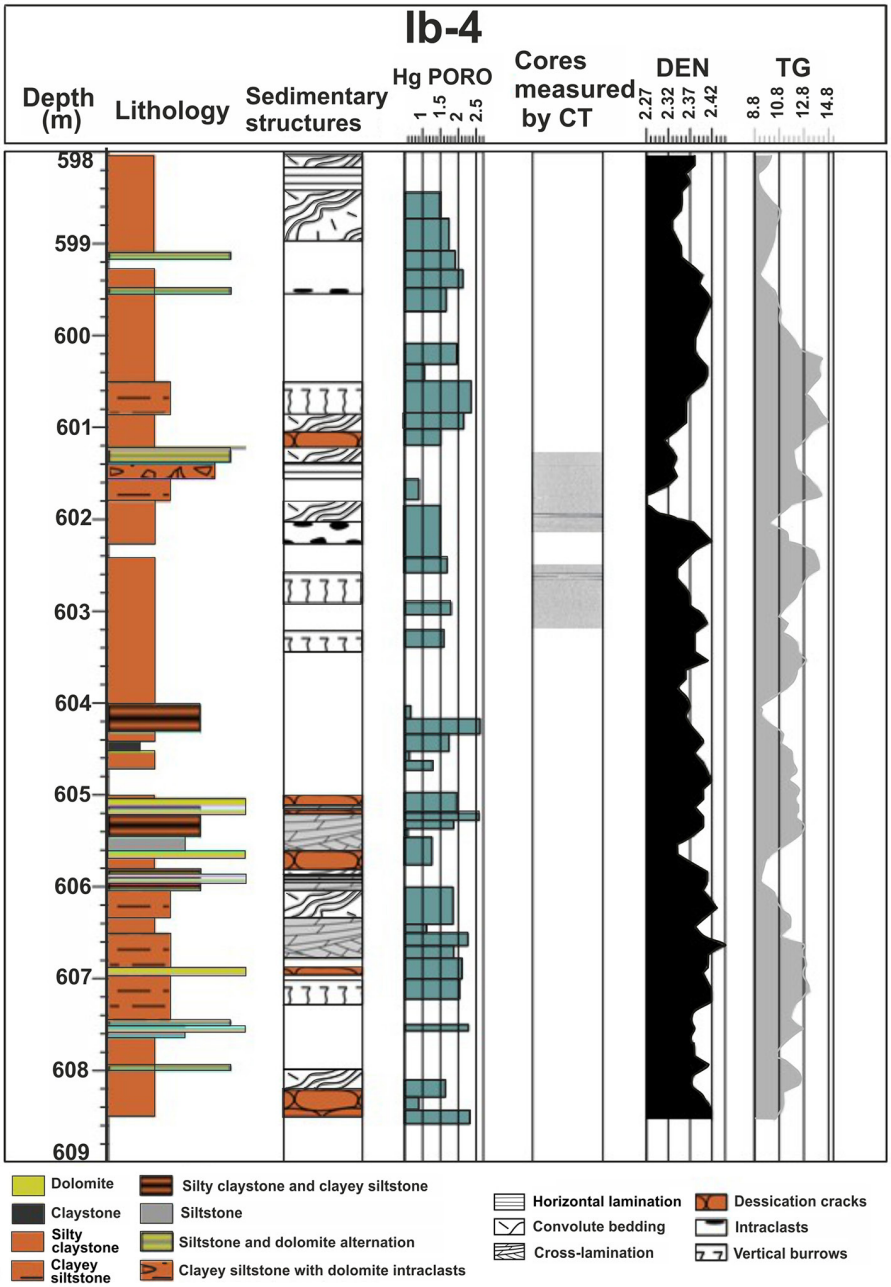

Fig. 3. The two cores studied by CT in the entire cored section of the well Ib-4. Abbreviations: Hg Poro = Mercury Porosity, Den = Density log, TG = Natural Gamma log.

Following the co-operation between the University of Szeged, GEOCHEM and the Public Limited Company for Radioactive Waste Management (PURAM), the raw data sets of dry and flooded CT measurements of 0.89 m and 10.54 m on the Ib-4 well material were transferred to the University of Szeged for further scientific research.

4. Methodology

Figure 4 outlines the workflow applied to obtain the REV of the core sample studied.

4.1. Pre-processing

A 3D-nearest neighbour algorithm was used to build the 3D volumes of the scanned dry core sample. This algorithm regulates the CT scan grids beneath each other to emulate the actual stratigraphical position. Although the output of computed tomography lends itself to straightforward interpretation, so-called scanning artifacts may obscure details of interest or cause the CT value of a single material to change in different parts of an image. The most commonly encountered artifact in CT scanning is beam hardening. Various methods have been developed to reduce or remove the effects of beam hardening (Van Geet et al., 2000: Ketcham & Carlson, 2001; Akin & Kovscek, 2003). One of these is the so-called "subset" CT volumes in which the image's outer edges are removed and only central volumes of the original three-dimensional images are used for quantitative analysis.

For the identification of rock-forming components of the core sample, CT HU intervals defined by PURAM for characteristic rock types of the BCF were used as follows: detrital fragments (coarse siltstone): <2700 HU, fine siltstone: 2700-3150 HU, claystone: 3150-3300 HU, calcite and /or dolomite: 3300-3600 HU, and albite: >3600 HU (Abutaha et al., 2021). The reality of the rock-forming components was compared with macroscopic core descriptions.

4.2. Quantitative analysis of CT volume

As X-ray attenuation is dependent on density, voxel values can be used to make millimetre-scale measurements of bulk density in a non-destructive way. In the present paper, we use the term density or CT-density as a synonym of HU. Calculation of the relative percentages of the rock-forming components for each layer was a requisite of the vertical subdivision of the studied core volume (Fig. 4). After averaging the compositional data by layers, the dominant rock-forming component lent the name of the rock type to the corresponding layer (Fig. 5; Table 1).

Linear correlation coefficients were calculated between any two pairs of rock-forming components averaged over a set of layers (Fig. 4). In the depiction of the correlation structure, the cutoff value was r2=|0.7|. That is, only those correlations where 50 per cent of the variance in a variable was predictable from the other one were regarded to be important relations.

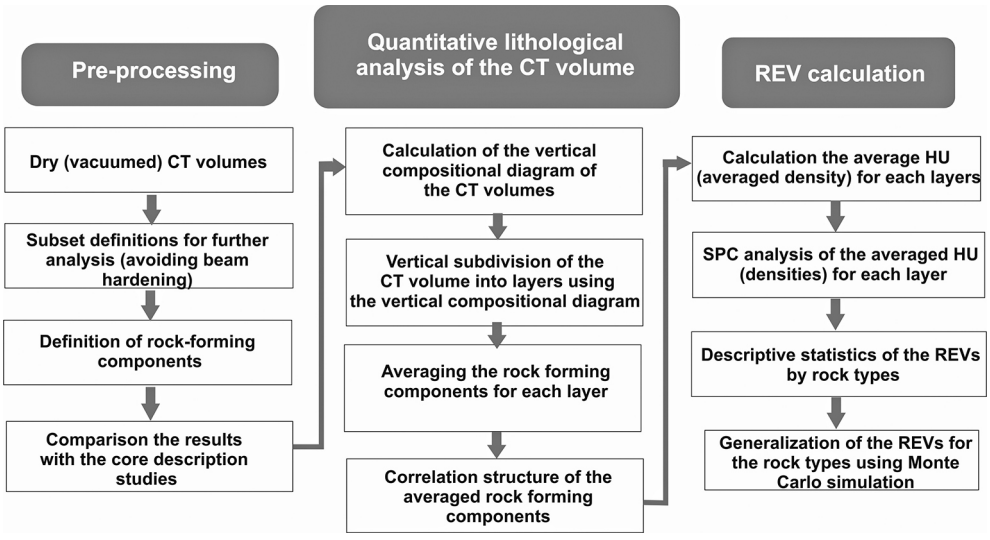

Fig. 4. The workflow.

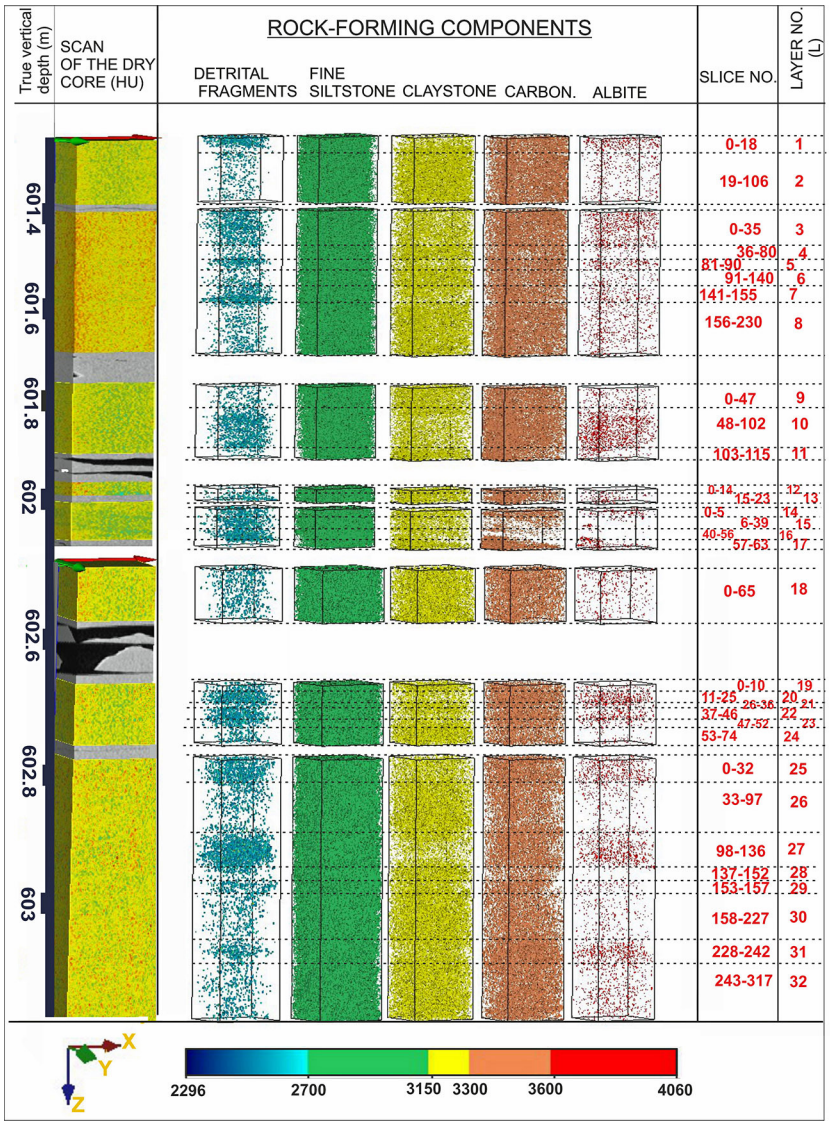

Fig. 5. Rock-forming components and boundaries of layers defined.

4.3. REV calculations

The REV for the layers chosen was performed by computing multiple incremental HU volumes in each layer. The process started with a cubic volume centred in the left-hand corner of the image. The volume was then expanded gradually by radial increments. The average of the acquired HU volumes was then computed and plotted on a chart of Statistical Process Control.

Statistical Process Control (SPC) is a family of methods to monitor and control a process using statistical methods (Shewhart, 1931; Montgomery, 1997; Oakland, 2003; Geiger, 2018). The objective was to detect anomalous values of the variable(s) analysed. In general, according to a certain tolerance margin and an objective value, two control limits, an upper control limit (UCL) and a lower control limit (LCL), are defined (Fig. 6).

Their practical definitions depend on the type of SPC applied. If the measurements are within the UCL and LCL, there is not a non-random pattern in the distribution, and the process is under statistical control (Fig. 6). However, if there are points (measurements) outside the limits, then for these points, the process is not controlled (Montgomery, 1997; Russo et al., 2012; Geiger, 2018).

From the model describing the change of average HU in the gradually increasing voxel volumes the "objective value" was derived. The tolerance margins, UCL and LCL, were calculated from the variance of actual data around the model curve. In

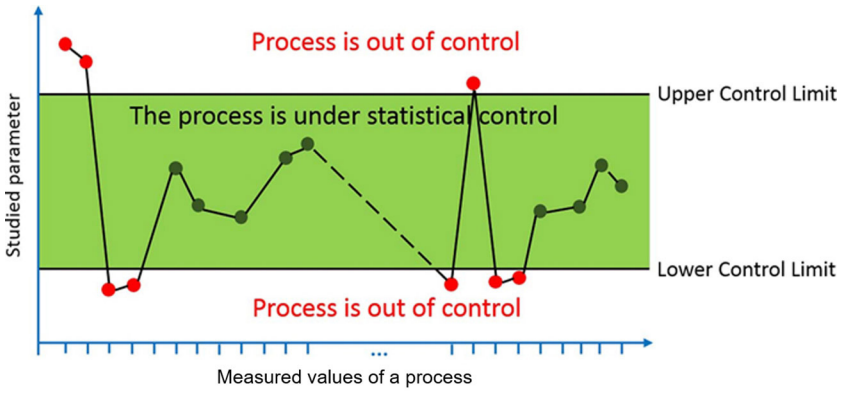

Fig. 6. The SPC chart.

this way, the REV was the voxel volume number of realisations from which all HU values ended up being controlled (Figs 6, 7D).

In general, the practice of SPC analysis consisted of three steps: understanding the process and specification limits, elimination of special sources of variations and monitoring the ongoing process (Polhemus 2005). In the present study, the last step is not used. Normally, SPC works under the assumption that the data observed are independent. However, in our case, a continuous transition violating independence between the different rock-forming components must be assumed. ARIMA (AutoRegressive Integrated Moving Average) charts are designed to handle suchsituations (e.g., Box et al., 1994; Polhemus, 2005; Russo et al., 2012). In their most general form, ARIMA (p, d, q) models consist of three characteristic terms: (1) a set of autoregressive terms (denoted by p), (2) a set of moving average terms or non-seasonal differences (denoted by d), and (3) a set of lagged forecast errors in the prediction equation (denoted by q). The general form of the model is as follows (Polhemus, 2005):

$$Yt = \mu + \varphi_1 Y_{t-1} + \varphi_2 Y_{t-2} + \ldots + \varphi_p Y_{t-p} + a_t - \theta_1 a_{t-1} - \theta_2 a_{t-2} - \ldots - \theta_q a_{t-q} \quad (3)$$

where μ is the constant, φ_k, is the autoregressive coefficient at lag k, θ_k, is the moving average coefficient at lag k, and a_{t-a} is the forecast error that was made at period . The ARIMA charts procedure creates control charts for a single numeric variable where data have been collected either individually (this version was used here) or in subgroups. The out-of-control signals are based on the deviations of the process from this dynamic time series model (Fig. 6). In this chart, the data are drawn around a centreline located at the expected value, μ, with control limits at

$$\mu \pm k \times \sigma^2 \quad (4)$$

In the present study, $k = 1$. The mean and standard deviation depend on the ARIMA model specification (Polhemus, 2005). Figure 7 demonstrates a typical example of the applied analysis with ARIMA charts for the first layer shown in Figure 5. In Figure 7A, the components of the fitted ARIMA (1,0,0) model are shown. The explicit form of this model is a linear combination of a constant, one autoregressive term, and an error term (Fig. 7B). The calculated centreline (average) and the UCL and LCL lines are shown in Figure 7C. Finally, in Figure 7D, the ARIMA chart can be seen, where the red dots indicate those parts of the series where severe deviations can be detected from the ARIMA (1,0,0) model (Fig. 7C). From the 15th incremental step, a series of averaged HU values are within the envelopes (UCL and LCL). That is, the CT densities are fully controlled. Consequently, the REV can be identified as the volume behind the 15th incremental step (1.25 cm^3).

Calculations detailed above were performed for each of the 32 layers. A particular REV value obtained may depend on the volume of the corresponding layer, which makes the comparison complicated. To circumvent this problem, the REV values were normalised by the corresponding layer volumes (Table 3). In this way, the REV could be expressed as the volume percentage of the studied subvolume (layer).

A Monte Carlo simulation uses repeated sampling to obtain the statistical properties of some phenomena. Gordon et al. (1993) published the first application of a Monte Carlo resampling algorithm in Bayesian statistical inference: the bootstrap filter. The bootstrap algorithm did not require any assumption about the state-space or the noise of the system.

A ARIMA(1,0,0) parameters

Parameter	Estimate	t-value	p-value
AR(1)	0.853	14.842	0.00
Mean	3149	136.306	0.00
Constant	463.50		

C ARIMA chart parameters

$UCL = CL + 0.5\sigma^2$	3158
$Centerline\ (CL)$	3149
$LCL = CL - 0.5\sigma^2$	3140

B The ARIMA(1,0,0) model

$$Y_t = 463.502 + 0.853 \cdot Y_{t-1} + e_t$$

D

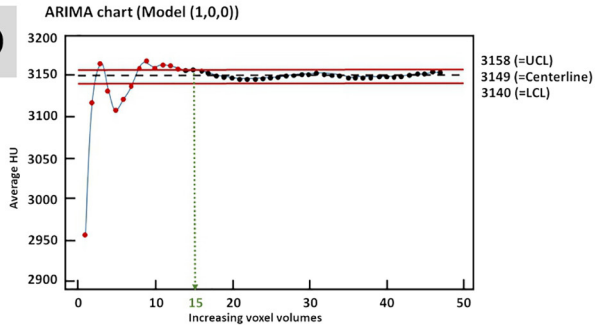

Fig. 7. An example of the applied ARIMA charts. **A –** Parameters of the selected model; **B –** The explicit form of the selected model; **C –** Parameters of the ARIMA chart; **D –** ARIMA chart with the indication of the volume step where the REV can be defined.

The Monte Carlo simulation focuses on constantly repeating random samples to achieve certain results. Once the simulation is complete, the results are averaged to provide an estimate. We applied this approach to simulate 1,000 outcomes of the REV calculated for each rock type. By doing so, we assumed that those parts of the core studied fairly and representatively described the composition of the rock types of the entire core (Table 4).

5. Results

5.1. Quantitative analyses of rock types

Based on the relative frequencies of compositional data, 32 thin layers (abbreviated as L) were defined throughout the 2-m core sample (Fig. 5; Table 1). Each 3D brick of the dry scans included five rock constituents. They were (1) detrital fragments (HU <=2700), (2) fine siltstone (2700 HU-3150 HU), (3) claystone (3150 HU-3300 HU), (4) dolomite, and calcite cement (3300 HU-3600 HU), and (5) albite (HU>3600). Based on the most frequent rock-forming constituent we could classify the stacked slices of CT volumes into relatively thin consecutive layers.

The layer-averaged compositional frequencies showed the variability of the fine siltstone component to be very high (from 39% in layer L17 to 64.84% in layer L27), while that of claystone is significantly smaller (from 29.6% in layer L27 to 39% in layer L2). The average carbonate content may vary between 10% (in layer L28) and 22.5% (in layer L10). The abundance of albite and detrital fragment constituents is relatively low; their averages do not exceed 1%. Based on the dominant rock-forming constituent, two rock types could be defined: clayey siltstone and fine siltstone (Table 1). The dominant sedimentary structures of the clayey siltstone layers are convolute laminations, desiccation cracks with diagenetic calcite precipitations and dolomite lenses. The fine siltstone layers are characterised by cross-laminations with parallel set boundaries, with abundant albite nests appearing on the bedding surfaces, as well as synsedimentary faults (Table 1).

The linear correlation coefficients calculated between each pair of the rock-forming components show a feedback system among the fine siltstone, claystone and carbonate components. In the feedback, the higher the fine siltstone frequency, the smaller the claystone and carbonate content. The albite can linearly be related only to the carbonate content (Table 2).

5.2. REV calculations of CT density

As shown in Table 3, the REV values range from 0.7514 cm^3 up to 13.1072 cm^3. The data of Table 3 show that the largest REV values correspond to the presence of sedimentary structures (e.g., L9 and L11 in Table 3). Alternatively, such large REVs can be related to the highest (> 60%) siltstone constituent (e.g., L15 and L16 in Table 3). It can also be conclud-

Table 1. Averaged compositional data by layers of the CT volumes.

Layer no.	Thickness (cm)	Averages of rock-forming components %					Rock type	Sedimentary features
		Detrital fragment	Fine siltstone	Claystone	Carbonate	Albite		
L1	2.250	0.544	47.604	32.289	19.192	0.371	Clayey siltstone	Dolomite intercalation, convolute bedding, vertically oriented calcite fillings
L2	10.875	0.048	41.532	39.763	16.612	0.045	Clayey siltstone	
L3	4.375	0.301	45.628	33.949	19.798	0.324	Clayey siltstone	
L4	5.500	0.145	47.600	35.599	16.518	0.138	Clayey siltstone	
L5	1.125	0.530	48.214	32.048	18.892	0.315	Clayey siltstone	
L6	6.125	0.147	47.899	35.980	15.894	0.081	Clayey siltstone	Dolomite lenses and horizontal laminations
L7	1.750	0.809	53.608	30.382	15.052	0.148	Fine siltstone	Abundant albite nests on bedding surfaces
L8	9.250	0.072	44.942	37.823	17.089	0.073	Clayey siltstone	
L9	5.875	0.079	43.774	38.021	18.021	0.104	Clayey siltstone	Desiccation cracks, intraclasts, and convolutions
L10	6.705	0.341	43.597	33.103	22.488	0.471	Clayey siltstone	
L11	1.500	0.045	44.656	38.405	16.849	0.046	Clayey siltstone	
L12	1.750	0.062	47.020	37.349	15.504	0.064	Clayey siltstone	Abundant albite nests on bedding surfaces
L13	1.000	0.326	53.564	31.943	14.041	0.126	Fine siltstone	
L14	0.625	0.589	50.354	31.935	16.803	0.319	Fine siltstone	Albite nests and aleurolit intraclasts
L15	4.125	0.354	63.610	27.558	8.362	0.097	Fine siltstone	
L16	2.000	0.920	64.843	23.764	10.409	0.065	Fine siltstone	
L17	0.750	0.062	39.236	38.707	21.802	0.192	Clayey siltstone	
L18	8.125	0.082	48.115	37.178	14.572	0.052	Clayey siltstone	Albite nests & cracks
L19	1.250	0.123	48.644	36.141	15.017	0.076	Clayey siltstone	
L20	1.750	0.497	48.266	31.281	19.537	0.419	Clayey siltstone	Mainly structureless, bioturbation and aleurolite intraclast can also be present
L21	1.250	0.239	49.636	33.639	16.030	0.160	Clayey siltstone	
L22	1.125	0.439	48.782	32.246	18.215	0.318	Clayey siltstone	
L23	0.625	0.277	51.159	33.376	15.081	0.107	Fine siltstone	
L24	2.625	0.084	51.264	36.645	11.980	0.027	Fine siltstone	
L25	4.000	0.345	48.948	32.976	17.488	0.241	Clayey siltstone	
L26	8.000	0.077	51.888	35.668	12.321	0.046	Fine siltstone	Crossbedding with parallel set boundaries, synsedimentary faults, abundant albite nests
L27	4.750	0.698	54.474	29.630	14.937	0.262	Fine siltstone	
L28	1.875	0.074	56.732	33.832	9.344	0.018	Fine siltstone	
L29	0.500	0.282	54.501	32.326	12.780	0.110	Fine siltstone	
L30	8.625	0.068	50.614	36.917	12.370	0.030	Fine siltstone	Crossbedding with parallel set boundaries, synsedimentary faults, abundant albite nests
L31	1.750	0.192	44.045	35.051	20.416	0.296	Clayey siltstone	Calcite precipitations in the cracks
L32	9.250	0.061	44.399	38.710	16.755	0.076	Clayey siltstone	

Table 2. The linear (Pearson) correlation coefficients for averaged HU data of rock-forming components. Between brackets, the $p < 0.05$ values indicate statistically significant non-zero correlations at the 95.0% confidence level.

	Detrital fragments	Fine siltstone	Claystone	Carbonate	Albite
Detrital fragments	1	**0.519** (p=0.002)	**−0.878** (p=0)	−0.012 (p=0.947)	**0.501** (p=0.004)
Fine siltstone		1	**−0.785** (p=0)	**−0.828** (p=0.303)	−0.253 (p=0.163)
Claystone			1	0.303 (p=0.091)	−0.352 (p=0.048)
Carbonate				1	**0.705** (p=0)
Albite					1

Table 3. Summary table of REV calculations.

Layer no.	Thickness of the layer (cm)	Volume of the layer (cm^3)	REV (cm^3)	Normalized REV (in the percent of the layer volume)	Rock type	Sedimentary structures
L1	2.25	22.48	1.3	5.78	Clayey siltstone	
L2	10.88	108.64	4.7	4.33	Clayey siltstone	
L3	4.38	43.71	2.1	4.80	Clayey siltstone	
L4	5.50	54.95	2.1	3.82	Clayey siltstone	
L5	1.13	11.24	3.0	26.69	Clayey siltstone	
L6	6.13	61.19	10.7	17.49	Clayey siltstone	Dolomite lenses and horizontal laminations
L7	1.75	17.48	1.1	6.29	Fine siltstone	Abundant albite nests on bedding surfaces
L8	9.25	92.41	2.8	3.03	Clayey siltstone	
L9	5.88	58.69	11.2	19.08	Clayey siltstone	Desiccation cracks, intraclasts, and convolutions
L10	6.75	67.43	11.2	16.61	Clayey siltstone	
L11	1.50	14.99	11.1	74.07	Clayey siltstone	
L12	1.75	17.48	0.7	4.00	Clayey siltstone	Abundant albite nests on bedding surfaces
L13	1.00	9.99	1.3	13.01	Fine siltstone	
L14	0.63	6.24	1.6	25.63	Fine siltstone	
L15	4.13	41.21	10.7	25.97	Fine siltstone	Albite nests and aleurolit intraclasts
L16	2.00	19.98	12.6	63.06	Fine siltstone	
L17	0.75	7.49	2.2	29.36	Clayey siltstone	
L18	8.13	81.17	13.1	16.14	Clayey siltstone	Albite nests and cracks
L19	1.25	12.49	2.5	20.02	Clayey siltstone	
L20	1.75	17.48	2.0	11.44	Clayey siltstone	Mainly structureless, bioturbation and aleurolite intraclast can also be present
L21	1.25	12.49	2.6	20.82	Clayey siltstone	
L22	1.13	11.24	2.0	17.80	Clayey siltstone	
L23	0.63	6.24	1.4	22.42	Fine siltstone	
L24	2.63	26.22	1.5	5.72	Fine siltstone	
L25	4.00	39.96	2.2	5.51	Clayey siltstone	
L26	8.00	79.92	11.8	14.76	Fine siltstone	Crossbedding with parallel set boundaries, synsedimentary faults, with abundant albite nests
L27	4.75	47.45	9.5	20.02	Fine siltstone	
L28	1.88	18.73	1.1	5.87	Fine siltstone	
L29	0.50	5.00	1.1	21.93	Fine siltstone	
L30	8.63	86.16	11.8	13.74	Fine siltstone	Crossbedding with parallel set boundaries, synsedimentary faults, with abundant albite nests
L31	1.75	17.48	1.1	6.53	Clayey siltstone	Calcite precipitations in the cracks
L32	9.25	92.41	2.7	2.94	Clayey siltstone	

Table 4. Summary statistics of actual and simulated REV values of clayey-siltstone and fine siltstone layers.

Summary statistics	A	B	C	D
	REV (cm^3)	Normalized REV (%)	Monte Carlo simulation of the REV (cm^3) 1,000 runs	Monte Carlo simulation of the normalized REV (%) 1,000 runs
Clayey siltstone (N=20)				
Avg.	4.57	15.51	5.86	19.88
STD	4.18	16.11	4.57	17.76
Min.	0.70	2.94	0.70	2.94
Max.	13.10	74.07	13.10	74.07
Fine siltstone (N=12)				
Avg.	5.46	19.87	6.54	22.84
STD	5.20	15.49	5.14	15.84
Min.	1.10	5.72	1.10	5.72
Max.	12.60	63.06	12.60	63.06

ed that the average REV of the fine siltstone layers is larger than that of clayey siltstone layers. The former is 5.46 cm^3, the latter 4.57 cm^3 (Table 4, columns A and B).

Monte Carlo simulation with 1,000 runs was used to simulate the long-run properties of REV and the normalised REV for both lithologies. The results are summarised in Table 4 (columns C and D). In the studied core volume, the average REV of the CT density of clayey siltstone is slightly smaller (5.86 cm^3) than that of fine siltstone (6.54 cm^3). In the case of clayey siltstone, the normalised REV is 19.88% of the studied subvolume (on the scale of the studied core volume) on average, while this value is 22.84% for fine siltstone.

6. Discussion

Spatial variations in CT densities (HU) can be used to identify small-scale textural and structural heterogeneities in rocks. According to our findings, the calculated REV of CT-densities (HU values) can be directly related to the high textural heterogeneity caused by the sedimentary structures. Figure 8 shows four high-resolution CT images of convolute lamination (Fig. 8A), a mud intraclast (Fig. 8B), a crack (Fig. 8C) and a pair of cross laminae. The high and low-density components are very close to one another. The density contrast is high even within a short distance. In such situations, the series of the average CT densities of the increasing volumes show a monotonously increasing pattern until the volume does not cover the entire sedimentary structure. The normalised REV values are below 10% whenever the corresponding layer does not show any sedimentary structure (Table 3).

Our study was based on the statistical analysis of vacuumed CT scans. Consequently, in the validation of results, the effect of vacuuming on the integrity of core samples, specifically minerals (such as clay) that contain water as part of their crystal struc-

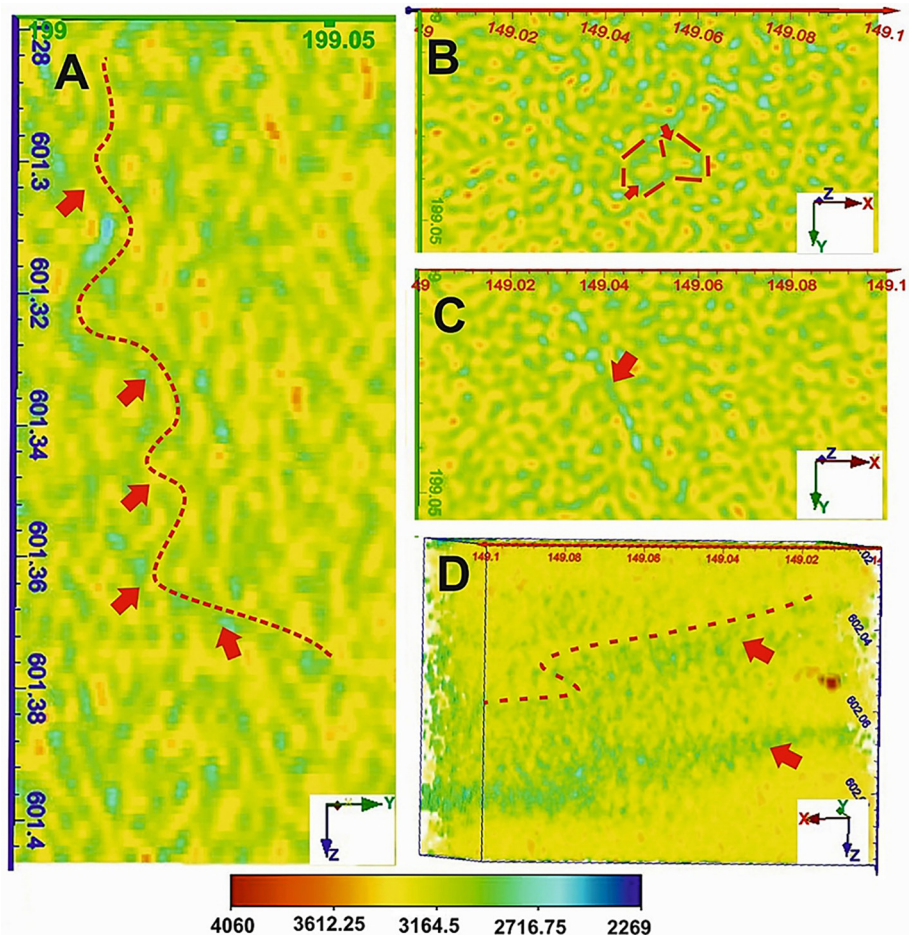

Fig. 8. Sedimentary features of the defined layers. **A –** Convolute lamination; **B –** Mud intraclast; **C –** Crack; **D –** Cross-lamination. Red dashed lines show the sedimentary structure out-borders and red arrows point out the actual deformation positions.

ture, must be considered. Various illite and illite/smectite-mixed assemblages constitute the dominant clay minerals of the Boda Claystone Formation (Németh & Máthé, 2016). Clay minerals are present as part of rock fragments, "allogenic clays" or authigenic clays (Abutaha et al., 2021). Partial to complete albitisation of detrital plagioclase of the BCF yielded Ca^{2+} to react with HCO^{3-} and Mg^{2+}(+Fe^{2+}) to produce carbonate cement (Table 2; the positive relationship between albite and carbonate is ~0.7).

Bush & Jenkins (1975) reported that the drying process of core samples in an unhumidified oven will remove not only the free pore water but also the layers of non-liquid water from the clay minerals. They pointed out that, because this water is an integral part of the clays in the reservoir, removing it during laboratory drying will increase the available pore space and cause erroneously high porosity measurements. Different clay minerals exhibit different levels of sensitivity to drying, with smectite-type clays being the most sensitive and kaolinite the least (Keelan, 1982). The presence of smectite clay in narrow, slot-like flow channels, combined with its tendency to collapse when water is removed, may also cause large permeability (Soeder, 1986).

By comparing the highest and lowest ratios of the claystone rock-forming components layers in Table 1, we would obtain L9 and L16 layers. L9 has the highest claystone (38.02%) and smallest fine siltstone (43.77%) percentages, it includes desiccation crack and convolution, as deformation structures. In contrast, L16 shows the highest fine siltstone ratio (around 65%) and the lowest claystone percentage (23.76%) with a non-sedimentary structure realised. In layer L9, desiccation cracks are the dominant sedimentary structures. In this layer, the illite-smectite and smectite might be regarded as allogenic clay having been precipitated in mud cracks. Therefore, additive pore space resulting from clay shrinkage (during the drying process) might cause erroneously high porosity measurements, resulting in higher REV. In contrast, the clay in L16, which might be allogenic or/and authigenic and even be collapsed during the drying process, would not influence the inherent pore space ratio because of its low percentage. Studying the porosity distribution of the current BCF core sample, Abutaha et al. (2021) managed to confirm collapses of smectite/illite structures during the drying/saturation process and postulated sedimentary structures, i.e., convolute structures, to act as significant porosity-improving factors.

In other words: the presence of structures (sedimentary structures or even cracks) within the BCF core sample is more commonly interpreted as a type of heterogeneity, regardless of how regular their distribution is. The concept of increased heterogeneity could be viewed as a sharp density change in the CT number across a particular small section of a core (layer). Furthermore, internal void space in the layer's sedimentary features could be the real reason behind the high HU density contrast and the REV elevation. However, the core sample drying (vacuumed) process should be realised as an essential factor for creating pores and yielding illusory higher porosity measurements (clay collapsed). Those additive theoretical pores are presumed to have occurred in all layers with sedimentary structures (mud-cracks, cross-bedding, convolution) and cracks. Since the clayey-silt layers (L15, L16) show the maximum siltstone ratios (>60%), minimum claystone proportion, and lack any sedimentary features, the high inherent porosity is expected to be accurate. The large REV defined can thus certainly be related to an actual pore heterogeneity.

7. Conclusions

CT scanning is a powerful imaging technique for studying and analysing specimens in 3D without destroying them. CT numbers can also be used to proxy bulk density and identify sediment changes within a core sample. The present study aimed to quantify and evaluate the minimum volume of a Boda Claystone Formation core sample that could capture a representative quantity of physical heterogeneity (i.e., density) using the ARIMA SPC technique.

Stacked slices of CT volumes were grouped into relatively thin consecutive layers; thirty-two layers were defined. After averaging the compositional data by layers, the dominant rock-forming component provided the rock type name, i.e., fine siltstone layer (>50% siltstone component). Linear correlation coefficients between the averaged rock-forming components pairs were also studied across the set of layers.

The REV for the chosen layers was performed by computing multiple incremental HU volumes in each layer. The average CT densities of the increasing volumes showed a monotonously increasing pattern until the volume did not cover the entire sedimentary structure. The concept of increased heterogeneity, therefore, could be viewed as a sharp density change in the CT number (HU) across a particular small section of a core (layer). That is, the REV of CT densities can be directly related to the high textural heterogeneity caused by sedimentary

structures, i.e., the largest REV values corresponded to the presence of sedimentary structure (e.g., L9 and L11), or such large REVs could be related to the largest (> 60%) siltstone constituent.

In general, the average REV of the fine siltstone layers was larger than that of clayey siltstone layers: 5.46 cm^3 and 4.57 cm^3, respectively. By normalising the REV values with the corresponding layer volumes, they could be expressed as volume percentage of the studied subvolume (layer).

The Monte Carlo simulation was used to simulate the long-run properties of REV and the normalised REV. As a result, the simulated REV (average) of the CT density of clayey siltstone was slightly smaller (5.86 cm^3) than that of fine siltstone (6.54 cm^3). Simulated percentages of the normalised REV values in clayey siltstone were 19.88% on average of the studied subvolume (on the scale of the studied core volume) and 22.84% for fine siltstone.

The presence of structures (sedimentary structures or cracks) within the BCF core sample is more commonly interpreted as a type of heterogeneity; the higher the heterogeneity, the higher REV. Seemingly, internal void space in the layers' sedimentary features might be the real reason for developing the high HU density contrast (increasing REV). We believe that the drying process of the core sample could essentially affect the available pore space and cause erroneous higher-porosity measurements (by collapsing clay), especially at sedimentary structures and cracks, where authigenic clay is expected to occur primarily.

Acknowledgements

We wish to acknowledge the Public Limited Company for Radioactive Waste Management (PURAM) for permitting the University of Szeged to use their data sets in scientific research work. This research has been sponsored by the Interdisciplinary Excellence Centre, Institute of Geography and Earth Sciences, Long Environmental Changes Research Team, Grants 20391-3/2018/ FEKUSTRAT and GINOP-2.3.2-15-2016- 00009 'ICER' of the European Union and the State of Hungary, Ministry of Human Capacities. Mecsekérc Ltd financed the measurements, while cofinancing came from the European Regional Development Fund.

References

Abutaha, S.M., Geiger, J., Gulyás, S. & Fedor, F., 2021. Evaluation of 3D small-scale lithological heterogeneities and pore distribution of the Boda Claystone Formation using X-ray computed tomography images (CT). *Geologia Croatica* 74/3. doi: 10.4154/gc.2021.17

Akin, S. & Kovscek, A.R., 2003. Computed tomography in petroleum engineering research. [In:] Mees, F., Swennen, R., Van Geet, M. & Jacobs, P. (Eds): Application of X-ray computed tomography in the geosciences. *Special Publication, Geological Society of London*, 215, 23–38.

Al-Raoush, R. & Willson, C.S., 2005. Extraction of physically-representative pore network from unconsolidated porous media systems using synchrotron microtomography, *Journal of Hydrology* 23, 274–299.

Árkai, P., Balogh, K., Demény, A., Fórizs, I., Nagy, G. & Máthé, Z., 2000. Composition, diagenetic and post-diagenetic alterations of a possible radioactive waste repository site: the Boda Albitic Claystone Formation, southern Hungary. Acta Geologica Hungarica 43, 351-378.

Balázs, G.Y.L., Lublóy, É. & Földes, T., 2018. Evaluation of concrete elements with X-Ray computed tomography. *Journal of Materials in Civil Engineering* 30, 1-9.

Barabás, A. & Barabás-Stuhl, Á., 1998. *Stratigraphy of the Permian formations in the Mecsek Mountains and its surroundings*. [In:] Stratigraphy of geological formations of Hungary. Geological and Geophysical Institute of Hungary, 187-215 (in Hungarian).

Baveye, P., Rogasik, H., Wendroth, O., Onasch, I. & Crawford, J.W., 2002. Effects of sampling volume on the measurement of soil physical properties: simulation with X-ray tomography data. *Measurement Science and Technology,* 13, 775–784.

Bear, J., 1972. *Dynamics of fluids in porous media*. Dover Publications Inc., New York, 764 pp.

Bear, J. & Bachmat, Y., 1990. *Introduction to Modeling of Transport Phenomena in Porous Media*. Kluwer Academic Press, Dordrecht, 575 pp.

Blum, P., Mackay, R., Riley, M. & Knight, J., 2007. Performance assessment of a nuclear waste repository: upscaling coupled hydro-mechanical properties for far-field transport analysis. *International Journal of Rock Mechanics and Mining Sciences* 42, 781–792.

Box, G.E.P., Jenkins, G.M. & Reinsel, G.C., 1994. *Time series analysis: Forecasting and control*. 3rd Edition. Prentice Hall, Englewood Cliff, New Jersey, 619 pp.

Brown, G.O., Hsieh, H.T. & Lucero, D.A., 2000. Evaluation of laboratory dolomite core sample size using representative elementary volume concepts, *Water Resources Research* 36, 1199–1208.

Bush, D.C. & Jenkins, R.E., 1975. Proper Hydration of Clays for Rock Property Determinations. *Journal of Petroleum Technology* 22, 800-804.

Chang, C.S. & Gao, J., 1995. Second-gradient constitutive theory for granular material with random packing structure, *International Journal of Solids and Structures,* 32, 2279–2293.

Clausnitzer, V. & Hopmans, J.W., 1999. Determination of phase-volume fractions from tomographic measurements in two-phase systems, *Advances in Water Resources* 22, 577–584.

Cnudde, V., Masschaele, B., Dierick, M., Vlassenbroeck, J., Van Hoorebeke, L. & Jacobs, P., 2006. Recent pro-

gress in X-ray CT as a geosciences tool. *Applied Geochemistry* 21, 826–832.

Cnudde, V., Dewanckele, J., De Boever, W., Brabant, L., De Kock, T., 2012. *3D* characterization of grain size distributions in sandstone by means of X-ray computed tomography. In: Sylvester, P. (Ed.), Quantitative Mineralogy and Microanalysis of Sediments and Sedimentary Rocks. *Mineralogical Association of Canada (MAC),* 42, 99–113.

Coles, M.E., Hazlett, R.D., Spanne, P., Soll, W.E., Muegge, E.L. & Jones, K.W., 1998. Pore level imaging of fluid transport using synchrotron X-ray microtomography. *Journal of Petroleum Science and Engineering* 19, 55–63.

Coles, M.E., Muegge, E.L. & Sprunt, E.S., 1991. Applications of CAT scanning for oil and gas-production research. *IEEE Transactions on Nuclear Science* 38, 510–515.

Cormack, A.M. & Hounsfield, G.N., 1989. *Physiology or medicine 1979: Press release*. Accessed April 21, 2018. https://www.nobelprize.org/nobel_prizes/medicine/ laureates/1979/press.html.

Duchesne, M.J., Moore, F., Long, B.F. & Labrie, J., 2009. A rapid method for converting medical Computed Tomography scanner topogram attenuation scale to Hounsfield Unit scale and to obtain relative density values. Engineering Geology 103, 100–105.

Feyel, F. & Chaboche, J.-L., 2000. FE2 multiscale approach for modelling the elasto-viscoplastic behavior of long fiber SiC/Ti composite materials. *Computer Methods in Applied Mechanics and Engineering* 183, 309–330.

Földes, T., 2011. Integrated processing based on CT measurement. *Journal of Geometry and Physics* 1, 23–41.

Földes, T., Kiss, B., Árgyelán, G., Bogner, P., Repa, I. & Hips, K., 2004. Application of medical computer tomography measurements in 3D reservoir characterization. *Acta Geologica Hungarica*, 47, 63–73.

Gang, W., Shen, J., Liu, Sh., Jiang, Ch., Qin, X., 2019. *Three-dimensional modeling and analysis of macro-pore structure of coal using combined X-ray CT imaging and fractal theory*. International Journal of Rock Mechanics and Mining Sciences,123,104082. https://doi.org/10.1016/j.ijrmms.2019.104082.

Garvey, C.J. & Hanlon, R., 2002. Computed tomography in clinical practice. *British Medical* Journal 324, 1077–1080.

Geiger, J., 2018. Statistical process control in the evaluation of geostatistical simulations. *Central European Geology,* 6/1, 50-72.

Gordon, N.J., Salmond, D.J. & Smith, A.F.M., 1993. Novel approach to nonlinear/non-Gaussian Bayesian state estimation, *IEE Proceedings F (Radar and Signal Processing)* 40, 107-113.

Haas, J.& Péró, C.S., 2004. Mesozoic evolution of the Tisza Mega-unit. *International Journal of Earth Sciences* 93, 297–313.

Heismann, B.J., Leppert, J. & Stierstorfer, K., 2003. Density and atomic number measurements with spectral x-ray attenuation method. *Journal of Applied Physics* 94, 2073-2079.

Herman, G.T., 2009. *Fundamentals of computerized tomography: Image reconstruction from projection*. 2nd ed., Springer, 300 pp.

Hounsfield, G.N., 1973. Computerized transverse axial scanning (tomography). 1. Description of system. *British Journal of Radiology* 46, 1016-1022.

Hove, A.O., Ringen, J.K. & Read, P.A. 1987.Visualization of laboratory corefloods with the aid of computerized tomography of X-rays. *Society of Petroleum Engineers Reservoir Engineering* 2, 148-154.

Keelan, D.K., 1982. Core analysis for aid in reservoir description. *Journal of Petroleum Technology* 34, 2483-2489.

Ketcham, R.A. & Carlson, W.D., 2001. Acquisition, optimization and interpretation of X-ray computed tomographic imagery: applications to geosciences. *Computational Geosciences* 27, 381–400.

Konrád, G.Y., Sebe, K., Halász, A. & Babinszki, E., 2010. Sedimentology of a Permian playa lake: The Boda Claystone Formation, Hungary. *Geologos* 16, 27–41.

Kouznetsova, V., Brekelmans, W.A.M. & Baaijens, F.P.T., 2001. An approach to micro–macro modelling of heterogeneous materials. *Computational Mechanics* 27, 37–48.

Kouznetsova, V., Geers, M.G.D. & Brekelmans, W.A.M., 2002. Multi-scale constitutive modelling of heterogeneous materials with a gradient-enhanced computational scheme. *International Journal for Numerical Methods in Engineering* 54, 1235–1260.

Long, J., Remer, J., Wilson, C. & Witherspoon, P., 1982. Porous media equivalents for networks of discontinuous fractures. *Water Resources Research* 18, 645–658.

Louis, L., Wong, T.F. & Baud, P., 2007. Imaging strain localization by X-ray radiography and digital image correlation: deformation bands in Rothbach sandstone. *Journal of Structural Geology* 29, 129–140.

Máthé, Z., 1998. Summary report of the site characterization program of the Boda Siltstone Formation. *Mecsek Ore Environment Company*, Pécs, 4.

Máthé, Z. & Varga, A., 2012. "Ízesíto" a permi Bodai Agyagko Formáció oskörnyezeti rekonstrukciójához: kosó utáni pszeudomorfózák a BAT-4 fúrás agyagkomintáiban. ["Seasoning" to the palaeoenvironmental reconstruction of the Permian Boda Claystone Formation: pseudomorphs after halite in the claystone samples of the deep drillings BAT-4]. *Földtani Közlöny* 142, 201-204 (in Hungarian with English summary).

Montgomery, D.C., 1997. *Introduction to Statistical Quality Control*. John Wiley and Sons, New York, 759 pp.

Muhlhaus, H.B. & Oka, F., 1996. Dispersion and wave propagation in discrete and continuous models for granular materials. *International Journal of Solids and Structures* 33, 271–283.

Németh, T. & Máthé, Z., 2016. Clay mineralogy of the Boda Claystone Formation (Mecsek Mts., SW Hungary). *Open Geoscience* 8, 259–274.

Oakland, J.S., 2003. *Statistical process control*. Butterworth-Heineman, Oxford, 460 pp.

Peerlings, R.H.J. & Fleck, N.A., 2001. Numerical analysis of strain gradient effects in periodic media. *Journal De Physique* IV, 11, 153–160.

Polhemus, N.W., 2005. *How to: Construct a control chart for autocorrelated data*. StatPoint Technologies, Herndon, 16 pp.

Russo, D. & Jury, W.A., 1987. A theoretical study of the estimation of the correlation scale in spatially varied fields, 2. Nonstationary fields. *Water Resources Research* 23, 1269–1279.

Russo, S.L., Camargo, M.E. & Fabris, J.P., 2012. *Applications of control charts ARIMA for autocorrelated data*. [In:] Nezhad, M.S.F. (Ed.): Practical Concepts of Quality Control. InTech, Rijeka, 31–53.

Shapiro, A.M. & Andersson, J., 1983. Steady state fluid response in fractured rock: a boundary element solution for a coupled, discrete fracture continuum model. *Water Resources Research* 19, 959–969.

Shewhart, W.A., 1931. *Economic control of quality of the manufactured product*. Van Nostrand, New York, 501 pp.

Soeder, D.J., 1986. Laboratory drying procedures and the permeability of tight sandstone core. *SPE Formation Evaluation* 1, 16-22.

Sutton, S.R., Bertsch, P.M., Newville, M., Rivers, M., Lanzirotti, A. & Eng, P., 2002. Microfluorescence and microtomography analyses of heterogeneous earth and environmental materials. *Reviews in Mineralogy and Geochemistry* 49, 429–483.

Taud, H., Martinez-Angeles, T.R., Parrot, J.F. & Hernandez-Escobedo, L., 2005. Porosity estimation method by X-ray computed tomography. *Journal of Petroleum Science and Engineering* 47, 209 – 217.

Van Geet, M., Swennen, R. & Wevers, M., 2000. Quantitative analysis of reservoir rocks by microfocus X-ray computerised tomography. *Sedimentary Geology* 132, 25–36.

Van Kaick, G. & Delorme, S., 2005. Computed tomography in various fields outside medicine. *European Radiology* 15, D74–D81.

Varga, A.R., Szakmány, G.Y., Raucsik, B. & Máthé, Z., 2005. Chemical composition, provenance and early diagenetic processes of playa lake deposits from the Boda Siltstone Formation (Upper Permian), SW Hungary. *Acta Geologica Hungarica* 48, 49–68.

Vinegar, H.J., Wellington, S.L., 1987. Tomographic imaging of three-phase flow experiments. Review of Scientific Instruments. 58 /1, 96–107.

Webster, R., 2000. Is soil variation random? *Geoderma* 97, 149–163.

Wesolowski, J.R. & Lev, H.M., 2005. CT: History, technology, and clinical aspects. *Seminars in Ultrasound, CT and MRI* 26, 376–379.

Withjack, E.M., 1988. Computed tomography for rock property determination and fluid flow visualization. *SPE Formation Evaluation* 3, 696-704.

Manuscript submitted: 15 August 2021
Revision accepted: 28 October 2021